nature communications

Article

https://doi.org/10.1038/s41467-026-71730-3

# Oxidation-reconstructed $Li^+$ transport enables high-tap-density single-crystal regeneration of spent $LiNi_{0.5}Co_{0.2}Mn_{0.3}O_2$ positive electrodes

Received: 1 July 2025

Accepted: 30 March 2026

Published online: 14 April 2026

Check for updates

Shuaipeng Hao[1], Yi Zhang[1], Shuaiwei Liu[2], Zhouliang Tan[3], Wei Liu[4], Yuanguang Xia[5,6], Wen Yin[5,6], Yaqi Liao[1], Haijin Ji[1], Yuelin Kong[1], Yudi Shao[1], Yuelin Lv[1], Long Qie[1] ✉, Yunhui Huang[1] ✉ & Lixia Yuan[1] ✉

Direct regeneration offers a shortcut to close the material supply loop of lithium-ion batteries and is a promising recycling strategy. However, in spent $LiNi_{0.5}Co_{0.2}Mn_{0.3}O_2$ positive electrode, severe bulk cation disorder and surface rock salt phase hinder $Li^+$ reinsertion. Moreover, the coexistence of single and poly-crystal particles in commercial batteries further complicates uniform re-lithiation and morphological regeneration. Herein, we propose an oxidation strategy to simultaneously regulate the structural reconstruction and morphological evolution of spent material. During oxidation, surface NiO transforms into NiOOH, while targeted oxidation of the anti-site $Ni^{2+}$ to $Ni^{3+}$ in the bulk reduces $Li^+/Ni^{2+}$ mixing. This reconstructs $Li^+$ diffusion channels from surface to bulk, facilitating re-lithiation. Meanwhile, structural changes induce lattice expansion in secondary particles, causing their decomposition into primary particles and forming uniform precursor particles. These particles, with continuous $Li^+$ transport channels and NiOOH surface, agglomerate into large single-crystal during calcination. The regenerated $LiNi_{0.5}Co_{0.2}Mn_{0.3}O_2$ achieves a high tap density of 2.57 g/cm$^3$ and retains 80.2% capacity after 600 cycles. This work presents a concept for the direct regeneration of degradable positive materials.

Lithium-ion batteries (LIBs), valued for their high energy density and long cycle life, are extensively used in electric vehicles and grid-scale energy storage, resulting in a rising volume of spent LIBs[1–4]. Accordingly, efficient recycling of spent batteries, driven by environmental protection and resource reuse, is now a primary focus in industry and academia[5–7]. Current LIBs recycling relies primarily on pyrometallurgy, hydrometallurgy, or their combinations. Metallurgy routes, which break the chemical bonds of electrode materials and thus release valuable lithium and transition metals, are recognized as "down-cycling" strategies[8,9]. Besides, metallurgy routes generally require high

[1]State Key Laboratory of New Textile Materials and Advanced Processing, School of Materials Science and Engineering, Huazhong University of Science and Technology, Wuhan, Hubei, China. [2]Karlsruhe Institute of Technology (KIT), Institute for Applied Materials (IAM), Hermann-von-Helmholtz-Platz 1, D-76344 Eggenstein-Leopoldshafen, Karlsruhe, Germany. [3]State Key Laboratory of Chemistry and Utilization of Carbon Based Energy Resources, College of Chemistry, Xinjiang University, Urumqi, Xinjiang, China. [4]School of Automobile and Transportation Engineering, Guangdong Polytechnic Normal University, Guangzhou, China. [5]Institute of High Energy Physics Chinese Academy of Sciences, Beijing, P. R. China. [6]China Spallation Neutron Source Science Center, Dongguan, P. R. China. ✉e-mail: qie@hust.edu.cn; huangyh@hust.edu.cn; yuanlixia@hust.edu.cn

https://doi.org/10.1038/s41467-026-71730-3

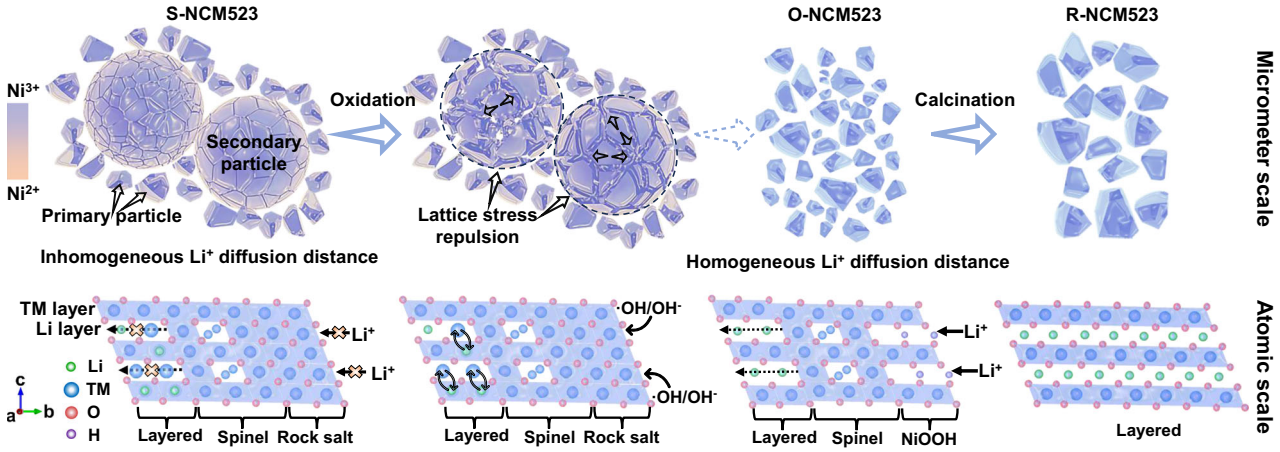


**Fig. 1 | Oxidation-enabled direct regeneration of S-NCM523 into single-crystal R-NCM523.** At the micrometer scale, mixed spent primary and secondary particles undergo oxidative reconstruction into uniform primary particles, followed by calcination into regenerated single-crystal NCM523. At the atomic scale, oxidation removes the rock-salt phase and cation disorder, reopening $Li^+$ diffusion channels, and subsequent calcination to reconstruct the layered structure.

temperatures or strong acids/alkalis, leading to high energy costs and secondary pollution[10,11]. In contrast, the direct regeneration route aims to repair defects in spent positive electrodes and restore their electrochemical performance without destroying the original crystal structure, which provides a shortcut to close the material supply loop of LIBs as a simpler, less polluting, and higher-value recycling method[12–14].

However, the direct regeneration of spent $LiNi_xCo_yMn_zO_2$ (NCM) positive electrodes is hampered by sluggish and heterogeneous $Li^+$ diffusion and poor morphology controllability, arising from intrinsic structural degradation and particle heterogeneity. During cycling, intrinsic structural instability drives Ni migration from the transition-metal (TM) layer to the Li layer, leading to severe $Li^+/Ni^{2+}$ mixing and surface degradation, particularly the formation of rock salt phase[15–17]. These degraded phases severely hinder $Li^+$ re-insertion and diffusion within the solid oxides, that is, the Li replenishment during regeneration[9,18]. In addition, to enhance compacted density and cycling stability, commercial NCM positive electrodes typically combine primary (single-crystal) and secondary (poly-crystal) particles. This heterogeneity varies $Li^+$ diffusion pathways among different particles, complicating uniform re-lithiation and morphologically homogeneous regeneration.

Currently, the direct regeneration of spent NCM primarily adopts hydrothermal or molten salt methods[16,19–22]. In the recovery process, to promote $Li^+$ insertion, high pressure and high lithium concentration are always required, which erodes economic profitability and increases the burden of pollution control[23,24]. Moreover, the hydrothermal re-lithiation can suffer from poor uniformity in Li replenishment due to differing diffusion paths within primary/secondary particles, undermining structural stability. The molten salt method is likely to induce anomalous growth of the original primary particles due to the addition of at least twice the lithium salt required for direct regeneration, thereby intrinsically limiting morphology controllability. Thus, although both methods enable relithiation, they rely on harsh conditions and struggle to balance structural repair with morphology regulation, making the efficient regeneration of NCM materials challenging.

As shown in Fig. 1, we propose an oxidation strategy based on $Na_2S_2O_8$ that can simultaneously address the above challenges under mild conditions. Strongly oxidizing $\cdot SO_4^-/\cdot OH$ radicals derived from $Na_2S_2O_8$ oxidize the surficial rock-salt NiO into a layered β-NiOOH phase, thereby establishing two-dimensional $Li^+$ diffusion channels. Meanwhile, in the bulk, the anti-site $Ni^{2+}$ in $LiO_6$ octahedron is oxidized to $Ni^{3+}$, which reverts to the $TMO_6$ octahedron due to its smaller radius and charge balance, significantly reducing $Li^+/Ni^{2+}$ mixing and repairing the $Li^+$ diffusion pathway. Furthermore, the increase in $Ni^{3+}$ in the bulk phase and the surface transition NiO to β-NiOOH jointly induce lattice expansion, driving secondary particles to disintegrate into uniform primary "precursors". These "precursor" features continuous $Li^+$ transport channels and a NiOOH-layered surface, enabling their coalescence into large single-crystals during subsequent calcination.

The regenerated single-crystal $LiNi_{0.5}Co_{0.2}Mn_{0.3}O_2$ (NCM523) exhibits a reversible discharge capacity of 144.2 mAh/g at 1 C, with capacity retention as high as 80.2% after 600 cycles. Notably, the oxidation strategy is also applicable to the direct regeneration of spent $LiNi_{0.6}Co_{0.2}Mn_{0.2}O_2$ (S-NCM622) and $LiNi_{0.8}Co_{0.1}Mn_{0.1}O_2$ (S-NCM811), yielding uniform single-crystal particles with high structural order and electrochemical stability. We anticipate that this oxidation strategy will inspire future research on the recycling of spent positive electrode materials and deepen understanding of the structure-recovery mechanism in spent NCM materials.

## Results

### Screening oxidants to achieve $Ni^{2+}$ to $Ni^{3+}$

To choose a proper oxidant, the Eh-pH phase diagram of the Ni-$H_2O$ system is constructed, as shown in Fig. 2a. An alkaline environment (pH=14) is predefined to prevent transition metal dissolution. The diagram reveals that NiO transforms into the layered NiOOH phase when the redox potential exceeds 0.54 V at pH=14, whereas the $Co_3O_4$ phase remains stable (Supplementary Fig. 1a). Meanwhile, to oxidize the bulk $Ni^{2+}$, an $E^o$ of ~2.50 V is required[25]. Standard electrode potentials of the typical oxidizing agents, calculated using the Nernst equation[26–28], are shown in Fig. 2b. Only $\cdot SO_4^-/\cdot OH$ radicals generated by the decomposition of $S_2O_8^{2-}$ are available to satisfy the oxidative demands of both surface and bulk phases. The presence of $\cdot SO_4^-/\cdot OH$ radicals during oxidation is confirmed by ESR testing (Supplementary Fig. 1b).

As shown in Fig. 2c, with $Na_2S_2O_8$ as an oxidizing agent, the surface NiO is converted to NiOOH, accompanied by a significant increase in the lattice spacing from 2.40 Å to 4.83 Å; the anti-site $Ni^{2+}$ in the $LiO_6$ octahedron, which has higher activity, is also oxidized to $Ni^{3+}$ and hence returns to the $TMO_6$ octahedron due to the radius variation and charge balance, causing c-axis expansion. The surficial and internal phase transitions induce lattice distortions, which increase the internal stresses within secondary particles, prompting their fragmentation into primary particles. The fragmentation unifies the morphology and homogenizes the $Li^+$ diffusion channels, further paving the way for subsequent Li replenishment.

https://doi.org/10.1038/s41467-026-71730-3

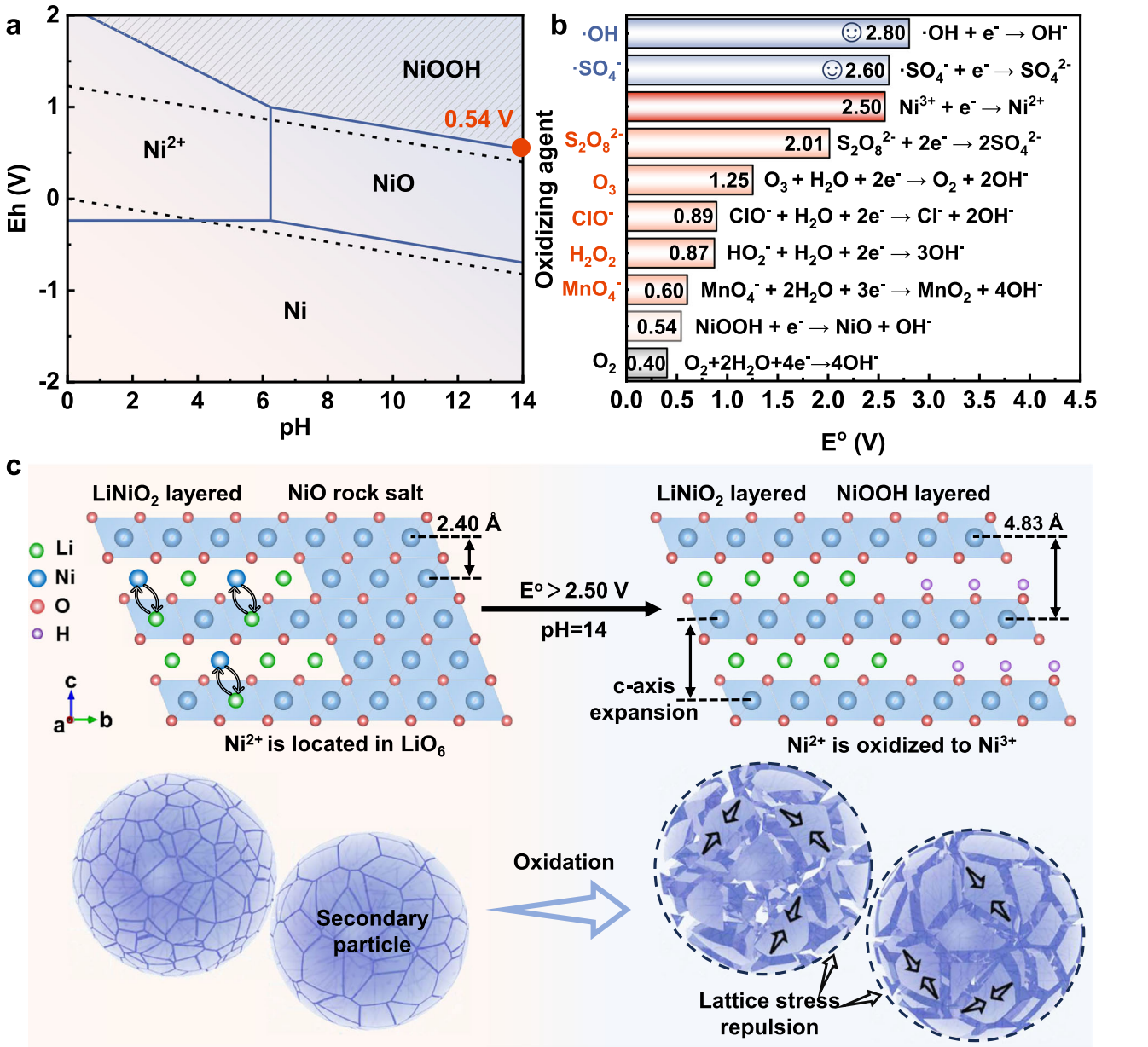


**Fig. 2 | Oxidation mechanism of O-NCM523. a** Eh-pH diagrams of the Ni-$H_2O$ system (273.15 K, 1 mol/kg). **b** Standard electrode potentials calculated from the Nernst equation for oxidizing agents (273.15 K, pH=14). **c** Schematic diagram of $Ni^{2+}$ oxidation to $Ni^{3+}$ triggering atomic rearrangement and stress-induced particle fragmentation in S-NCM523.

## Oxidation mechanism of S-NCM523

With spent NCM523 as a paradigm, the regeneration process involves two steps: (1) oxidation of spent NCM523 (denoted as S-NCM523, consisting of single and poly-crystal particles), where the as-obtained product is denoted as O-NCM523; (2) the subsequent high-temperature calcination of O-NCM523 with $LiOH{\cdot}H_2O$ as Li source, where the as-obtained product is denoted as R-NCM523. The initial pouch cell performance of S-NCM523 is shown in Supplementary Fig. 2. Additionally, regeneration via direct Li replenishment using a simple calcination route was conducted, and the product was used as a control sample (D-NCM523) to understand the role of the oxidation process.

As shown in Supplementary Table 1, R-NCM523 demonstrates a Li/TM molar ratio of 1.05, consistent with that of commercial NCM523. Neutron pair distribution function (NPDF) testing was employed to clarify the atomic-scale structural evolution from S-NCM523 to O-NCM523. As shown in Fig. 3a, d1-d5 correspond to the nearest in-plane TM-O and TM-TM atom pairs. NPDF refinement in Fig. 3b reveals that O-NCM523 and S-NCM523 have similar d1-d5 peaks in the 1–6 Å range, indicating a similar crystal framework. While meticulous comparisons reveal that the TM-O (d1, 2.055 Å) and TM-TM (d2, 2.925 Å) bonds of O-NCM523 are shorter than those of S-NCM523, reflecting stronger interatomic interactions associated with the oxidation of TM from lower to higher valence states. Additionally, the intensity of the d1 peak in O-NCM523 is lower than that in S-NCM523, which is due to the higher $Ni^{3+}$ content in O-NCM523 (less $Li^+/Ni^{2+}$ mixing), enhancing the Jahn-Teller effect and weakening the symmetry of the TM-O bond[29].

X-ray photoelectron spectroscopy (XPS) tests with different etching times were used to determine the oxidation of which specific TM elements in NCM. As shown in Supplementary Fig. 4, for S-NCM523, the Ni $2p_{3/2}$ peak shifts from 853.2 eV to 854.7 eV with increasing etching time, indicating the presence of surface degradation zones corresponding to NiO rock-salt phases. In contrast, for O-NCM523, the Ni $2p_{3/2}$ peak at 854.7 eV remains consistent from the

https://doi.org/10.1038/s41467-026-71730-3

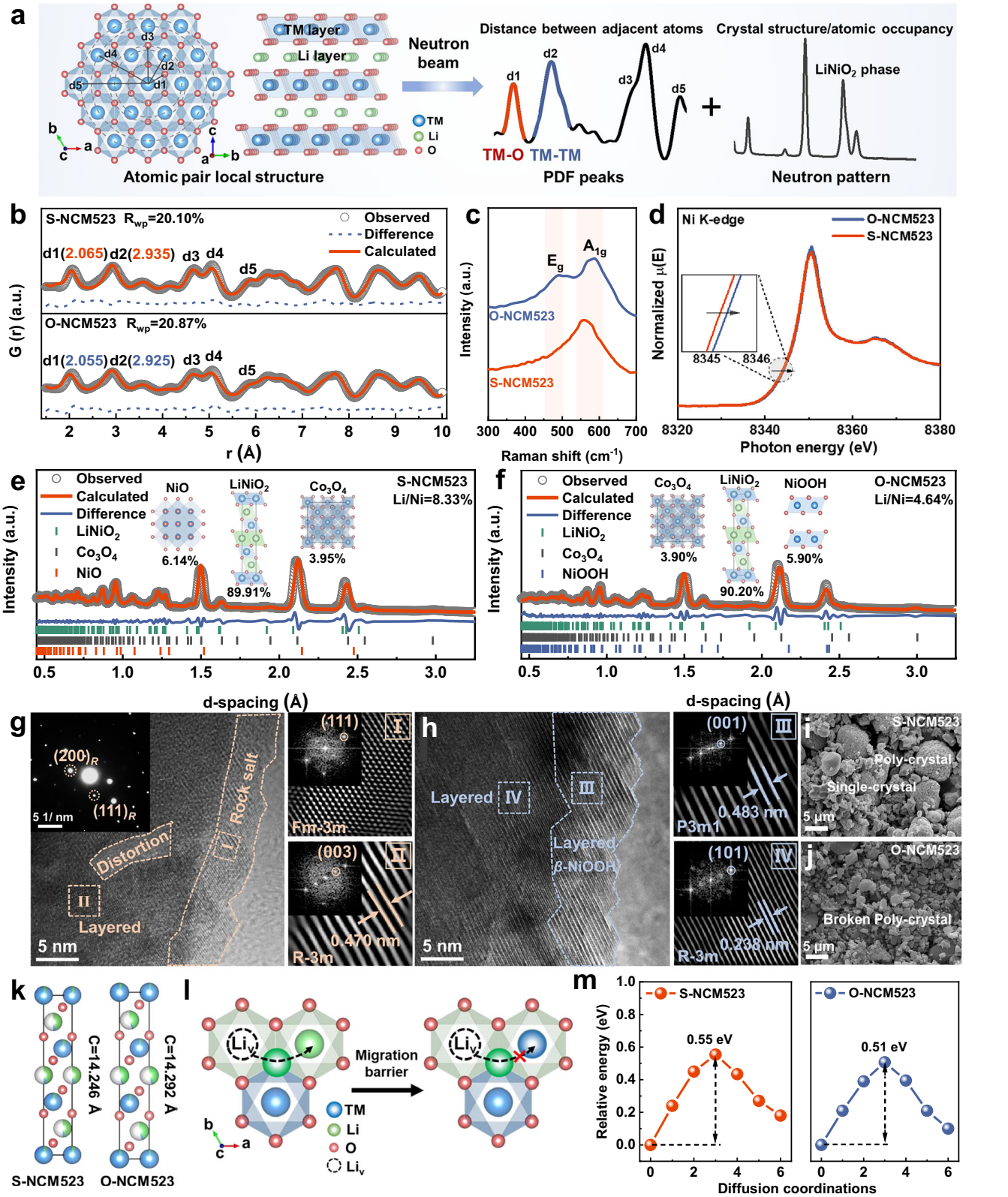


**Fig. 3 | Structure and morphology evolution from S-NCM523 to O-NCM523.** **a** Schematic diagram of the NCM crystal structure corresponding to the NPDF and NPD characteristic peaks. **b** NPDF refinement patterns of S-NCM523 and O-NCM523. **c** Raman spectra of S-NCM523 and O-NCM523. **d** Normalized Ni K-edge XAFS spectra of S-NCM523 and O-NCM523. **e, f** NPD refinement patterns of S-NCM523 and O-NCM523. **g, h** HRTEM images of S-NCM523 and O-NCM523. **i, j** SEM images of S-NCM523 and O-NCM523. **k** Schematic diagram of the lattice parameter c of S-NCM523 and O-NCM523. **l**, Schematic diagram of $Li^+$ diffusion pathways. **m** Relative energy for $Li^+$ diffusion of S-NCM523 and O-NCM523.

surface to the near-surface region. Obviously, the oxidation process promotes the conversion of Ni (II) to Ni (III) as expected. Meanwhile, the valence states of Co and Mn remain unchanged (Supplementary Fig. 5a–d). Moreover, Raman spectra in Fig. 3c show only $A_g$ signals in S-NCM523, confirming the presence of surface NiO phase[30]. In contrast, O-NCM523 exhibits both $A_{1g}$ and $E_g$ signals, suggesting the formation of a layered structure on the surface. Subsequently, as shown in Fig. 3d, X-ray absorption near-edge structure (XANES) spectroscopy was used to probe Ni valence states in the bulk of S-NCM523 and O-NCM523. The Ni K-edge spectra of O-NCM523 exhibit a clear shift to higher energies. Meanwhile, the extended X-ray absorption fine structure (EXAFS) Fourier transform reveals that the Ni-O and Ni-TM bond lengths in O-NCM523 are shorter than those in S-NCM523, and the Ni-TM peak intensity in O-NCM523 is weaker than in S-NCM523 (Supplementary Fig. 5e), suggesting the elimination of the NiO phase[31,32]. Collectively, these results confirm that the oxidation mechanism primarily targets the oxidation of $Ni^{2+}$ in S-NCM523.

The evolution of the bulk $Li^+/Ni^{2+}$ mixing and surface rock salt phase in S-NCM523 after oxidation was determined by neutron powder diffraction (NPD) refinement. As shown in Fig. 3e, f, the $Li^+/Ni^{2+}$ mixing decreases from 8.33% in S-NCM523 to 4.64% in O-NCM523. This is attributed to the oxidation of $Ni^{2+}$ in $LiO_6$ to $Ni^{3+}$, which has a smaller radius (0.56 Å) than $Li^+$ (0.76 Å) and tends to migrate from $LiO_6$ back to $TMO_6$[33]. Meanwhile, the NiO phase in S-NCM523 transforms into NiOOH during oxidation, and the NiOOH content in O-NCM523 is 5.90%, with both $R_{wp}$ (5.87%) and $R_F$ (5.40%) values below 10% (Supplementary Tables 12 and 13), indicating good reliability of the fitting. Moreover, after removing the NiOOH phase during refinement of NPD and NPDF, the $R_{wp}$ values increase to 7.69% and 26.40%, respectively, further confirming the existence of the NiOOH phase in O-NCM523 (Supplementary Fig. 6). XPS analysis further confirms this transformation. The O1s XPS spectra in Supplementary Fig. 7a reveal the formation of NiOOH on the O-NCM523 surface. The Ni 2p XPS spectra in Supplementary Fig. 7b show a higher fraction of Ni (III) in O-NCM523 than that in S-NCM523, indicating the surface transformation from NiO to NiOOH.

All reactions related to the oxidation-derived regeneration process are outlined in Supplementary Table 2. To further verify the transformation from the tough rock-phase NiO to layered NiOOH, $Na_2S_2O_8$ solution was reacted with NiO. As shown in Supplementary Fig. 8, after 1 h of reacting at 25°C, NiOOH diffraction peaks appear, confirming that the surface NiO in S-NCM523 could be directly transformed into NiOOH by $Na_2S_2O_8$.

The $Li^+$ loss during the oxidation process was quantified by ICP analysis. Comparable $Li^+$ loss was observed across S-NCM523 samples subjected to different oxidation times. As shown in Supplementary Table 3, Li loss stabilizes after the reaction time reaches 1 h. The final Li/TM ratio of O-NCM523 is slightly lower than that of S-NCM523 (0.5), indicating a limited Li loss during oxidation. These results indicate that the oxidation reaction proceeds rapidly and causes negligible structural damage.

The effects of $Na_2S_2O_8$ concentration, pH, temperature and reaction time on the oxidation process are summarized in Supplementary Tables 3, 25–29 and Supplementary Fig. 9. For spent samples subjected to the same oxidation treatment, those with lower anti-site $Ni^{2+}$ content exhibit less $Ni^{2+}$ oxidation and smaller changes in $Li^+/Ni^{2+}$ mixing and Li/TM ratio (Supplementary Fig. 10a–e and Tables 3, 30–34). This indicates that Li loss during oxidation is positively correlated with the amount of anti-site $Ni^{2+}$ (Supplementary Fig. 10f). This correlation arises because the anti-site $Ni^{2+}$ occupies a distorted $NiO_6$ octahedron with longer, weaker Ni-O bonds and an unstable coordination environment[34,35]. Consequently, its electrons are more easily extracted by oxidizing agents, leading to oxidation to $Ni^{3+}$. Samples with fewer anti-site $Ni^{2+}$ are more structurally stable, reducing the likelihood of $Ni^{2+}$ oxidation and consequently weakening the $Li^+$ loss and structural changes.

The oxidation also induces fragmentation of the secondary particles of O-NCM523. As shown in Fig. 3g, the high-resolution transmission electron microscopy (HRTEM) image of S-NCM523 shows a lattice spacing of 2.39 Å in region I near the surface, corresponding to the rock-salt phase, as confirmed by SAED. Figure 3h shows a layered structure on the O-NCM523 surface (region III) with a lattice fringe spacing of 4.83 Å, corresponding to the (001) plane of β-NiOOH (space group P3m1)[36,37]. Region IV, with a lattice spacing of 2.40 Å, corresponds to the (101) plane of $LiNiO_2$. These observations confirm the oxidation of surface NiO to NiOOH. Scanning electron microscopy (SEM) verifies that the secondary particles in S-NCM523 (Fig. 3i) fragment into primary particles after oxidation (Fig. 3j). Two main factors drive the fragmentation of secondary particles. First, the oxidation from $Ni^{2+}$ to $Ni^{3+}$ in the bulk causes partial $Li^+$ extraction to maintain charge balance. The removal of $Li^+$ increases the negative charge density of the oxygen layers, thereby strengthening the electrostatic repulsion between adjacent oxygen layers[38]. Consequently, the lattice parameter c of O-NCM523 increases to 14.292 Å, higher than the 14.246 Å of S-NCM523 (Fig. 3k). Second, the surface phase transition from NiO to layered β-NiOOH significantly expands the surface lattice spacing (2.40 Å to 4.83 Å). These changes increase stress between the primary particles, fragmenting secondary particles into primary particles. The regularized particle morphology homogenizes the $Li^+$ diffusion paths and distances during subsequent re-lithiation. Moreover, based on the density functional theory (DFT) calculation, the $Li^+$ diffusion energy barrier in O-NCM523 (0.51 eV) is lower than that in S-NCM523 (0.55 eV), as shown in Fig. 3l, m.

## Regeneration mechanism of O-NCM523

Subsequently, S-NCM523 and O-NCM523 were calcined at 900 °C for 10 h to obtain D-NCM523 and R-NCM523, respectively. As shown in Fig. 4a, as compared to the characteristic NPDF peaks before annealing, the r values of d1-d5 decrease after high-temperature Li replenishment, indicating that TM is oxidized to a higher valence state. Meanwhile, meticulous comparison shows that R-NCM523 restores the crystal structure's order more effectively than D-NCM523. The TM-O bond length in R-NCM523 is 1.945 Å, which is shorter than that in D-NCM523 (1.995 Å), suggesting more complete oxidation of $Ni^{2+}$. Moreover, the d1 peak intensity of R-NCM523 is lower than that of D-NCM523, indicating a stronger Jahn-Teller effect and lower $Li^+/Ni^{2+}$ mixing. Therefore, the $Li^+$ diffusion barrier of R-NCM523 (0.41 eV) is lower than that of D-NCM523 (0.48 eV), as shown in Fig. 4b. NPD refinements reveal specific $Li^+/Ni^{2+}$ mixing, with R-NCM523 at 2.06%, which is less than the 3.50% in D-NCM523 (Fig. 4c, d and Supplementary Tables 14 and 15). This is consistent with the NPDF and X-ray diffraction (XRD) results (Supplementary Fig. 11 and Tables 20–24), indicating that R-NCM523 has a highly ordered layered structure.

Furthermore, the HRTEM image in Fig. 4e shows that the lattice spacing of R-NCM523 is 4.70 Å (regions V and VI) in both the surface and bulk phases, corresponding to the (003) plane of $LiNiO_2$, with the SAED pattern confirming the regeneration of the layered structure. These results demonstrate that high-temperature $Li^+$ replenishment restores the degraded NCM523 crystal structure. XPS peak positions and intensities for Ni, Co, Mn, and O remain constant from surface to bulk in R-NCM523 (Supplementary Fig. 12), and the $A_{1g}$ and $E_g$ characteristic peaks of R-NCM523 in the Raman spectra are sharper than those of D-NCM523 (Supplementary Fig. 13), indicating more complete restoration of composition and layered ordering after calcination. This improvement arises from reduced $Li^+/Ni^{2+}$ mixing in the bulk phase of O-NCM523 and the conversion of the surface rock-salt phase to the layered NiOOH, which together facilitate $Li^+$ reinsertion into the layered structure during subsequent calcination.

https://doi.org/10.1038/s41467-026-71730-3

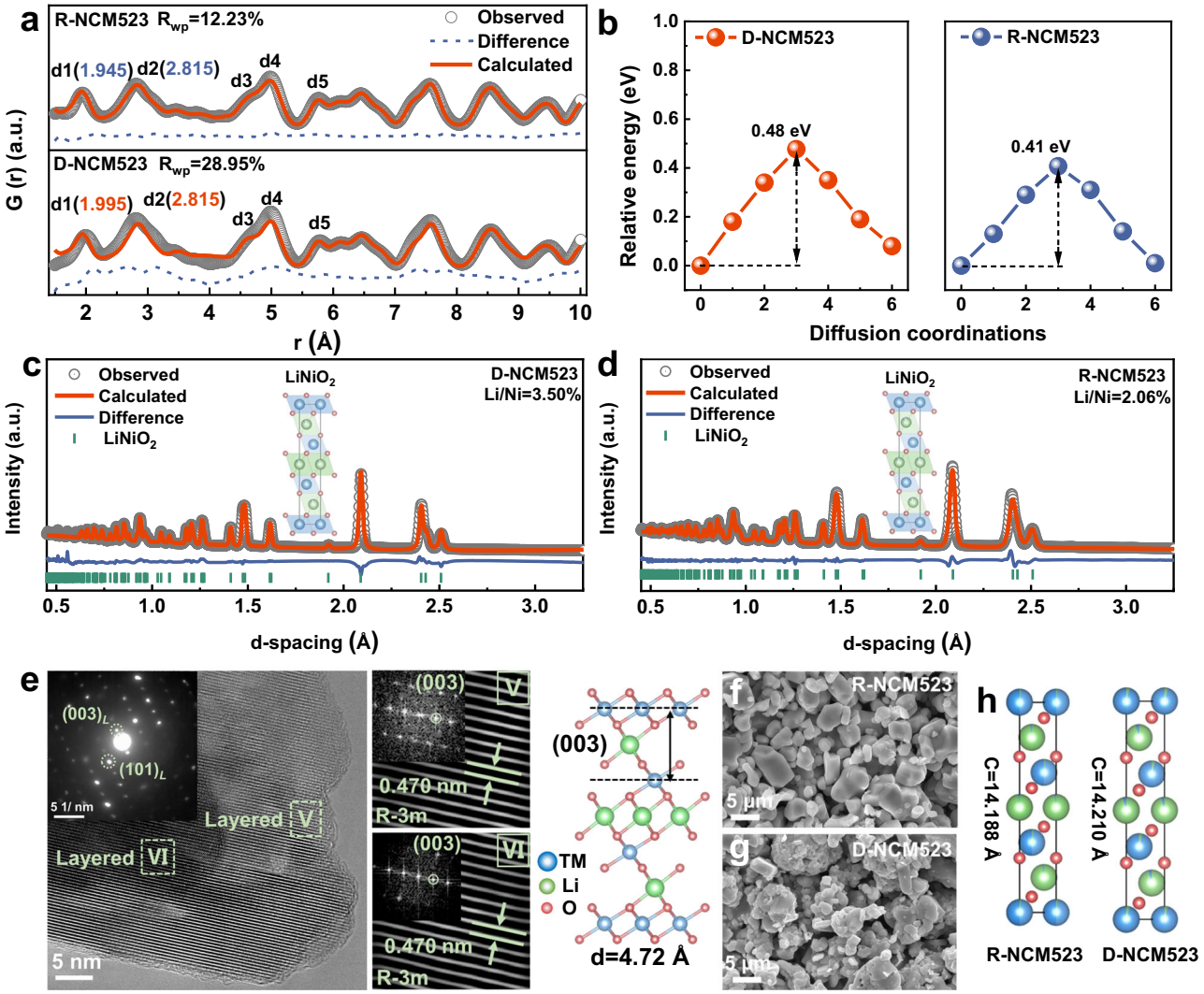


**Fig. 4 | Structure and morphology evolution of D-NCM523 and R-NCM523.** **a** NPDF refinement patterns of D-NCM523 and R-NCM523. **b** Relative energy for $Li^+$ diffusion of D-NCM523 and R-NCM523. **c**, **d** NPD refinement patterns of D-NCM523 and R-NCM523. **e** HRTEM images and SAED patterns of R-NCM523. **f**, **g** SEM images of D-NCM523 and R-NCM523. **h** Schematic diagram of the lattice parameter c of D-NCM523 and R-NCM523.

It is underscored that the pre-oxidation-supported R-NCM523 exhibits not only a unified single-crystal morphology but also a rare large size. To investigate the uniformity of elemental valence states within the particles, as shown in Supplementary Fig. 14, Electron energy loss spectroscopy (EELS) measurements were performed on different regions of the particles. The O K-edge and Ni L-edge spectra exhibit consistent peak positions and intensities, with no detectable Ni reduction or oxygen vacancy defects, indicating uniform elemental valence states within the particles. The SEM image in Fig. 4f clearly shows that R-NCM523 consists of primary particles with flat, smooth surfaces, regular shapes, and a size of 3–7 μm. Meanwhile, R-NCM523 reaches a high tap density of 2.57 g/cm$^3$ (Supplementary Table 5), significantly higher than that of commercial single-crystal NCM523 (CS-NCM523, ~1.62 g/cm$^3$, ~2.57 μm, Supplementary Fig. 15a, b). This structural feature originates from the NiOOH-layered surface formed on O-NCM523. DFT calculations show that the energy barrier for $Li^+$ migration from $Li_2O$ to NiO is 8.85 eV, whereas the barrier from $Li_2O$ to NiOOH is only 1.89 eV (Supplementary Fig. 17), indicating that the formation of NiOOH at the surface reduces the $Li^+$ diffusion barrier during calcination. Moreover, during low-temperature lithiation, NiOOH readily converts to layered $LiNiO_2$[39,40], whose lattice compatibility facilitates grain boundary fusion and promotes particle growth. By contrast, Fig. 4g shows irregular and agglomerated particles in D-NCM523, with a particle size of 5-10 μm. Additionally, the lattice parameter c of 14.188 Å for R-NCM523 is smaller than that of D-NCM523 at 14.210 Å (Fig. 4h), indicating that the layered structure of R-NCM523 is more stable.

## Microstructural evolution of O-NCM523 after high-temperature treatment

The subsequent high-temperature treatment also plays a key role in the structure recovery and the morphology control. Figure 5a shows the NPDF patterns at different regeneration temperatures, reacting to the changes of bond lengths between TM-TM and TM-O atoms, which are used to determine the oxidation state of the Ni element. The TM-O and TM-TM bond lengths gradually shorten as the regeneration temperature increases from 600 to 1000 °C, indicating the continuous increase of the oxidation state of Ni, and finally, the TM-O and TM-TM bond lengths shorten to 1.945 Å and 2.815 Å, respectively, at 900 °C. Moreover, an increased d4/d3 ratio and enhanced d5 intensity suggest higher TM occupancy in the second and third shells, correlated with reduced $Li^+/Ni^{2+}$ mixing[41]. Obviously, samples treated at 900 °C exhibit minimal $Li^+/Ni^{2+}$ mixing and maximal layered ordering (Fig. 5b).

Figure 5c shows the cation ordering degree and the change of lattice parameter c obtained from the refinement of NPD patterns at different regeneration temperatures, corresponding to the layered

https://doi.org/10.1038/s41467-026-71730-3

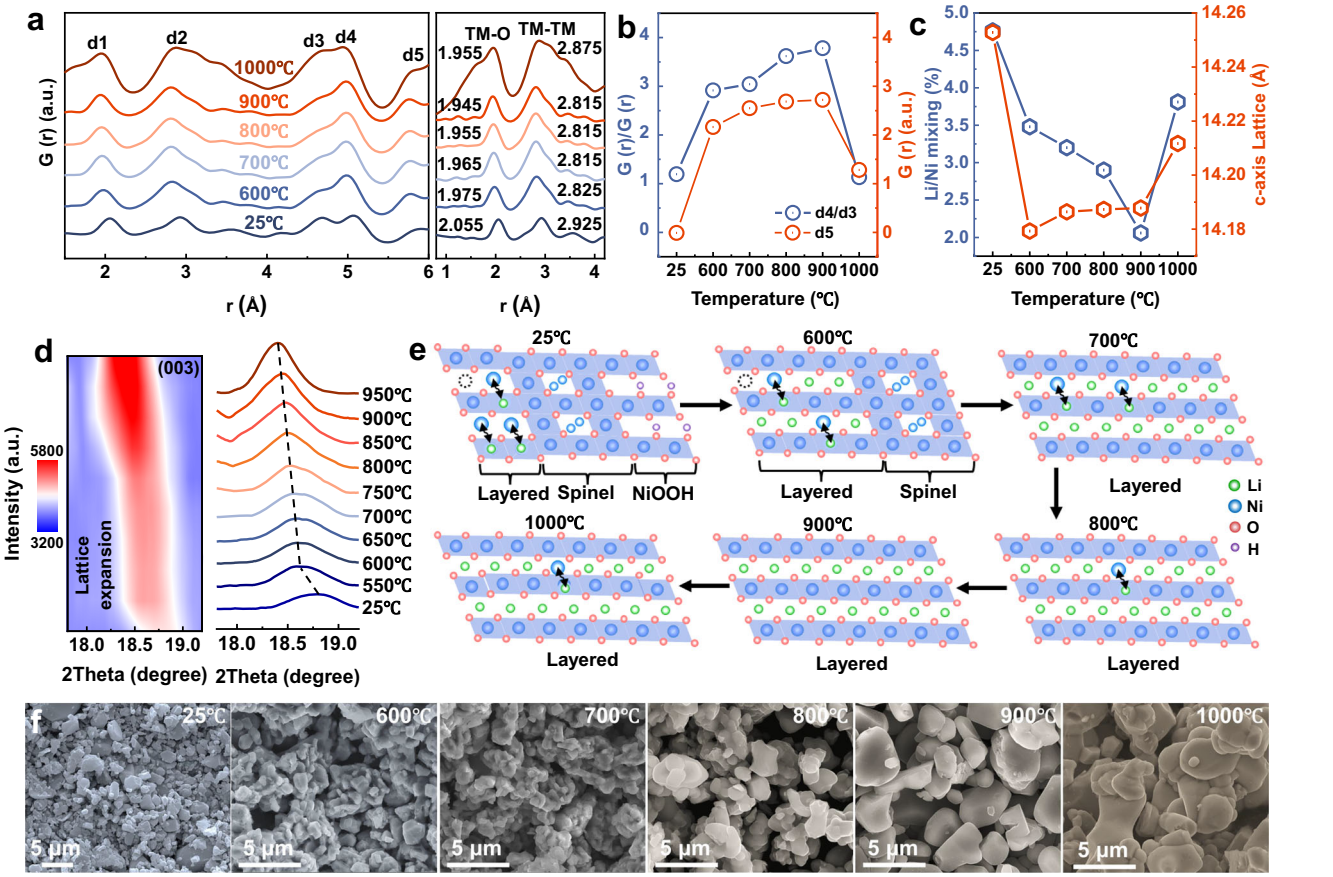


**Fig. 5 | Structure and morphology evolution of O-NCM523 after high-temperature treatment. a** NPDF pattern at different regeneration temperatures of O-NCM523. **b** Intensity of d5 peak and d4/d3 ratio at different regeneration temperatures of O-NCM523. **c** NPD refinement for $Li^+/Ni^{2+}$ mixing and lattice parameter c at different regeneration temperatures of O-NCM523. **d** High-temperature in-situ XRD patterns during direct regeneration of O-NCM523. **e** Crystal structure change at different regeneration temperatures of O-NCM523. **f** SEM images at different regeneration temperatures of O-NCM523.

structure ordering. Clearly, the degree of $Li^+/Ni^{2+}$ mixing decreases with increasing temperature, reaching a minimum of 2.06% at 900 °C, with a lattice parameter c of 14.188 Å. These results indicate that 900 °C is the optimal regeneration temperature, corresponding to the highest Ni oxidation state and the most ordered layered structure. For the 600 °C sample, there is still a residual 1.10% of the spinel phase, which fails to revert to a layered structure, ultimately leaving a 4.0% Li vacancy (Supplementary Fig. 20b and Table 16), and the above defects disappear when the regeneration temperature reaches 700 °C or above (Supplementary Fig. 20c, d and Tables 17, 18). At 1000 °C, oxygen vacancies form, lowering the $Li^+/Ni^{2+}$ migration barrier and facilitating $Li^+$ migration into the TM layer[42], thus intensifying the $Li^+/Ni^{2+}$ mixing to 3.81% (Supplementary Fig. 20f and Table 19) and lengthening the TM-O and TM-TM bond lengths. In O-NCM523 and its 600 °C regenerated samples, a multi-phase structure is observed, containing $LiNiO_2$, $Co_3O_4$, and NiOOH phases. The presence of multiple phases significantly affects the intensity of the short-range d1 peak in NPDF[43], rendering it unreliable for evaluating $Li^+/Ni^{2+}$ mixing. In contrast, the intensity of the long-range d3, d4, and d5 peaks is relatively less impacted by multiple phases, making them suitable for analyzing $Li^+/Ni^{2+}$ mixing.

In-situ and ex-situ temperature XRD tests further confirmed that the most ordered layered structure, along with the lowest $Li^+/Ni^{2+}$ mixing, was achieved at a regeneration temperature of 900 °C. As shown in Fig. 5d, the (003) peak shifts to lower angles with increasing sintering temperature, confirming successful $Li^+$ intercalation into the layered structure and layer spacing expansion, consistent with the NPDF and NPD results. But a clear $Li_2CO_3$ signal is observed below 600 °C (Supplementary Fig. 21), which results from the incomplete insertion of $Li^+$ into the layered structure and the consequent conversion of the remaining $Li_2CO_3$ on the surface of the particles. The recovery of the layered structure in NCM523 is reflected in the intensity ratio of the characteristic peaks (003) and (104)[44]. Clearly, the $I_{003}/I_{104}$ ratio reaches a maximum at 900 °C before decreasing at higher temperatures. SEM was employed to observe grain growth at different regeneration temperatures. As shown in Fig. 5f, at 600 °C, some $Li_2CO_3$ adheres to the particle surfaces, and the particle morphology does not change significantly compared to that of the precursor. As the temperature increases to 800 °C, fragmented particles fuse and grow into larger particles, approximately 1 μm in size. Optimal particle evolution occurs at 900 °C, where the particles are regularly shaped and range from 3–7 μm, exhibiting homogeneous dispersion. However, further heating to 1000 °C causes excessive grain boundary fusion, resulting in abnormal particle growth that severely hampers $Li^+$ extraction and insertion.

## Electrochemical performance

The electrochemical performances of S-NCM523 were systematically investigated. As shown in Fig. 6a, S-NCM523 has a discharge capacity of 42.8 mAh/g at 0.1 C, but after regeneration, the capacity of R-NCM523 is restored to 158.9 mAh/g, comparable to commercial NCM523 (C-NCM523). The galvanostatic intermittent titration (GITT) curve shows that S-NCM523 exhibits the highest polarization and overpotential during pulsed charge/discharge due to the severe structural degradation (Supplementary Fig. 22f). In contrast, the overpotential of

https://doi.org/10.1038/s41467-026-71730-3

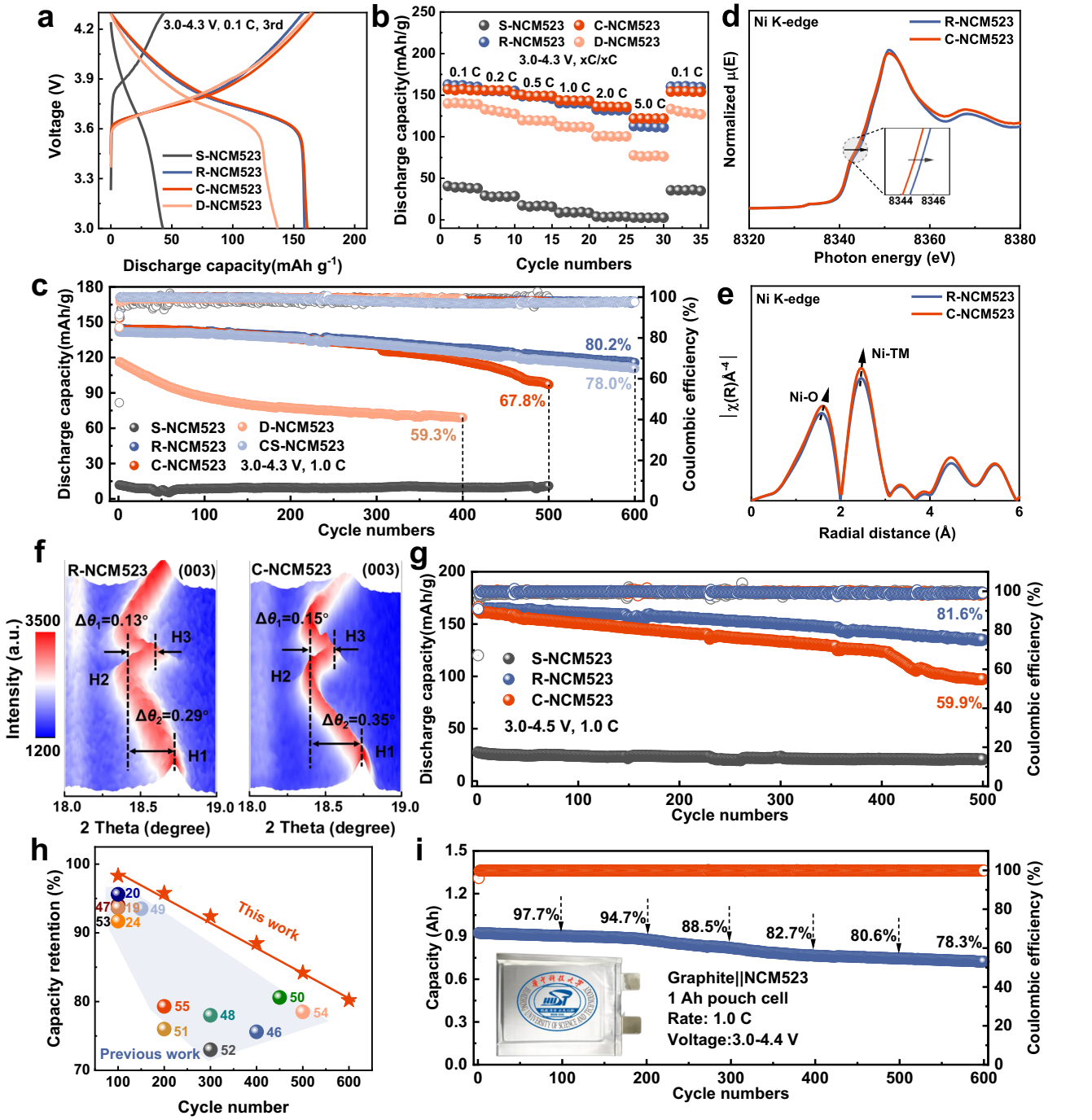


**Fig. 6 | Electrochemical performance of regenerated NCM. a** Charge and discharge curves of S-NCM523, R-NCM523, C-NCM523 and D-NCM523 at 0.1 C, 3-4.3 V (1 C = 170 mA/g). **b** Rate performance of S-NCM523, R-NCM523, C-NCM523 and D-NCM523 at xC, 3-4.3 V (x = 0.1, 0.2, 0.5, 1.0, 2.0 and 5, 1 C = 170 mA/g). **c** Cycling performance of S-NCM523, R-NCM523, C-NCM523, D-NCM523 and CS-NCM523 at 1.0 C, 3-4.3 V (1 C = 170 mA/g). **d**, **e** Normalized Ni K-edge XAFS and Fourier transform spectra of R-NCM523 (600 cycles) and C-NCM523 (500 cycles), measured at the discharged state (3.0 V) after cycling at 3.0-4.3 V, 1 C (1 C = 170 mA/g). **f** In-situ electrochemical XRD of R-NCM523 and C-NCM523 during cycling at 3.0-4.3 V, 0.2 C (1 C = 170 mA/g). **g** Cycling performance of S-NCM523, R-NCM523, and C-NCM523 at 3-4.5 V, 1 C (1 C = 170 mA/g). **h** Comparison of capacity retention between this work and representative reports (The source of the literature data listed in Supplementary Table 11). **i** Cycling performance of Graphite | |R-NCM523 pouch cell at 3-4.4 V, 1 C. All cells were tested at 25 ± 1 °C.

R-NCM523 (14.0 mV) is much lower than that of S-NCM523 (129.0 mV) and similar to C-NCM523 (14.0 mV).

R-NCM523 exhibits an excellent rate performance. It delivers capacities of 132.7 and 112.8 mAh/g at 2 and 5 C, respectively, close to that of C-NCM523 (Fig. 6b). At a low rate of 0.1 C, the capacity difference between D-NCM523 and R-NCM523 is ~17.0 mAh/g. As the rate increased, the capacity difference increased, too. At a 5 C rate, the capacity of D-NCM523 is ~35.0 mAh/g lower than that of R-NCM523. This can be attributed to the higher $Li^+/Ni^{2+}$ mixing and uneven particle size of D-NCM523, which blocks $Li^+$ diffusion pathways and increases the $Li^+$ diffusion distances. The electrochemical impedance spectroscopy (EIS) in Supplementary Figs. 23, 24 and the fitting data in Supplementary Tables 7–10 show that the interfacial impedance ($R_f$) and charge transfer impedance ($R_{ct}$) of R-NCM523 are significantly lower than those of S-NCM523 and D-NCM523, and close to C-NCM523. Cyclic voltammetry (CV) at a sweep rate of 0.1 mV/s demonstrates that

the redox peak difference of R-NCM523 is similar to that of C-NCM523 (Supplementary Fig. 25), indicating excellent electrochemical reversibility. In contrast, S-NCM523 and D-NCM523 show larger redox peak differences. Analysis of GITT and CV data shows that R-NCM523 and C-NCM523 have higher $Li^+$ diffusion coefficients, while S-NCM523 and D-NCM523 exhibit lower $Li^+$ diffusion coefficients (Supplementary Figs. 26, 22a–e).

As shown in Fig. 6c, R-NCM523 has a reversible discharge capacity of 144.2 mAh/g at 4.3 V, 1 C, with a high capacity retention of 80.2% after 600 cycles. R-NCM523 and C-NCM523 exhibit identical retention rates for the first 300 cycles, but C-NCM523 declines sharply due to secondary particle cracking (Supplementary Fig. 27), dropping to 67.8% after 500 cycles. CS-NCM523 maintains a capacity retention of 78.0% after 600 cycles, slightly lower than that of R-NCM523 (Supplementary Fig. 15d). This is attributed to the smaller particle size of CS-NCM523, which increases interfacial side reactions and undermines long-term structural stability[45]. D-NCM523 exhibits a capacity retention rate of only 59.3% after 400 cycles. As shown in Fig. 6d, XANES spectra identify the Ni chemical valence states of R-NCM523 and C-NCM523 after cycling. The Ni K-edge spectra of R-NCM523 shift to higher energies, suggesting a higher valence state of Ni in R-NCM523 than in C-NCM523 after cycling, with less $Li^+/Ni^{2+}$ mixing and rock salt. Meanwhile, EXAFS Fourier and wavelet transform analyses reveal shorter Ni-O and Ni-TM bonds in R-NCM523 than in C-NCM523 after cycling, suggesting better structural stability (Fig. 6e and Supplementary Fig. 29). In situ XRD analysis provides further insight into the excellent cycling stability of R-NCM523. As shown in Fig. 6f, for the (003) diffraction peak, the irreversible transition shift from H2 to H3 ($\Delta\theta1$) in R-NCM523 is 0.13°, which is lower than 0.15° in C-NCM523. A similar trend is observed for the (101) and (104) diffraction peaks (Supplementary Fig. 30a, b). In addition, at the end of charging, the lattice parameter changes of R-NCM523 ($\Delta c$ = 0.7%, $\Delta a$ = 1.0%) are less than those of C-NCM523 ($\Delta c$ = 1.0%, $\Delta a$ = 1.2%), indicating smaller lattice distortions, thus reduced accumulation of internal stresses during long cycling (Supplementary Fig. 30c, d). Therefore, R-NCM523 has excellent structural stability during charge/discharge cycling.

In addition, to further investigate the structural stability of R-NCM523, its cycling performance at high voltage (4.5 V) and high rate (5 C) was also tested. As shown in Fig. 6g, even after the voltage increases to 4.5 V, the retention rate is 81.6% after 500 cycles, which is much higher than the 59.9% of C-NCM523. R-NCM523 retains up to 72.5% of its capacity after 1000 cycles at 5 C, with a degradation rate of only 0.0275% per cycle (Supplementary Fig. 31). The above electrochemical performance indicates stable cycling performance for directly regenerated NCM materials (Fig. 6h, Supplementary Table 11)[19,20,24,46–55]. To validate the practical applicability of the regenerated positive electrode, a 1.0 Ah pouch cell was assembled using R-NCM523 as the positive electrode and graphite as the negative electrode. As shown in Fig. 6i, R-NCM523 exhibits stable cycling performance with a retention rate exceeding 78.3% after 600 cycles at 3.0-4.4 V, 1 C.

In addition, it is underscored that the pre-oxidation route can also regenerate S-NCM622 and S-NCM811, achieving retention rates of 79.1% for R-NCM622 and 77.6% for R-NCM811 after 200 cycles at 0.5 C (Supplementary Fig. 32). Moreover, the XRD refinement and ICP results for NCM622 and NCM811 samples before and after regeneration are shown in Supplementary Fig. 33 and Supplementary Tables 35–40. Thus, by using this proposed strategy, we successfully regenerated three degradable materials from different sources, all demonstrating excellent performance. This highlights the broad applicability of the proposed method and its great potential for practical use.

### Techno-economic analysis

The oxidation strategy offers several advantages. First, the regeneration process is concise, without requiring complex or hazardous devices. Second, it uses only conventional lithium salts, such as LiOH, reducing process costs. Third, $Na_2S_2O_8$ serves as the reagent in this method, and the subsequent addition of $Ca(OH)_2$ enables $SO_4^{2-}$ to precipitate as $CaSO_4$, minimizing environmental impact. Additionally, to further verify that no sulfur oxide species are released during the high-temperature regeneration process, TG-MS testing was conducted. The corresponding TG and MS signals are shown in Supplementary Fig. 34a, b. Over the entire temperature range from 30 to 900 °C, only signals at m/z = 18 ($H_2O$) and m/z = 44 ($CO_2$) are detected, corresponding to water release and the decomposition of $Li_2CO_3$, respectively. No signals at m/z = 64 ($SO_2$) or m/z = 80 ($SO_3$) are detected. The TG-MS results clearly indicate that no $SO_2$ or $SO_3$ is emitted during the high-temperature sintering of O-NCM523 regeneration. Therefore, the oxidation strategy offers advantages of high efficiency, low energy consumption, low emissions, and high profits.

The energy consumption of this method is 23.94 MJ/kg, and greenhouse gas (GHG) emissions are 3.11 kg/kg, both lower than those of the hydrothermal and molten salt methods, respectively (Supplementary Fig. 34c, d). Considering the comprehensive overall process costs, the oxidation method has a profit of $6.47/kg, which is 113.5% and 141.4% higher than the hydrothermal and molten salt methods, respectively (Supplementary Fig. 34e, f). In conclusion, compared to existing direct recycling technologies, the oxidation strategy has better capabilities in reducing GHG, lowering energy consumption, and enhancing profits. It provides an efficient, scalable solution for power battery recycling with broad industrial application potential.

## Discussion

We proposed a pre-oxidation strategy to regenerate spent single/polycrystal NCM523 into single-crystal NCM523. During oxidation, the bulk anti-site $Ni^{2+}$ in the $LiO_6$ octahedron is oxidized to $Ni^{3+}$, which reverts to the $TMO_6$ octahedron due to its smaller radius and charge balance, significantly reducing $Li^+/Ni^{2+}$ mixing and repairing the $Li^+$ diffusion pathway. Meanwhile, surface rock-salt NiO transforms into layered β-NiOOH, thus establishing two-dimensional $Li^+$ diffusion channels. Moreover, the bulk and surface structural changes induce lattice expansion and increase lattice stress within the secondary particles, leading to their self-decomposition into uniform primary precursor particles. These particles, featuring continuous $Li^+$ transport channels and NiOOH-layered surface, subsequently reaggregate into large single-crystals during calcination with a high tape density of 2.57 g/cm$^3$. R-NCM523 obtains a reversible discharge capacity of 144.2 mAh/g at 1 C. After 600 cycles, its capacity retention rate is 80.2%, with a capacity decay rate of only 0.033% per cycle. The strategy is also applicable to spent NCM622 and NCM811, enabling their efficient regeneration. This well-designed pre-oxidation strategy presents opportunities for recycling spent positive electrode materials.

## Methods

### Battery disassembly separation

Ten ~4 Ah spent $LiNi_{0.5}Co_{0.2}Mn_{0.3}O_2$ (S-NCM523) pouch cells were discharged by immersing them in 2 mol/L sodium chloride (NaCl, 99%, Aladdin) solution for 24 h. The cells were then manually disassembled to obtain the positive electrode. The positive electrode was cleaned with dimethyl carbonate (DMC, 99%, Aladdin) and dried. The S-NCM622 and S-NCM811 were obtained using the same method with spent commercial NCM622 and NCM811 pouch cells. Spent pouch cells from Nanjing Tongning New Materials Research Institute Co., Ltd.

### Direct regeneration process

S-NCM523 powder was placed in 0.5 mol/L sodium persulfate ($Na_2S_2O_8$, 99%, Aladdin) and 1.0 mol/L sodium hydroxide (NaOH, 98%, Aladdin). The solution was stirred at 400 rpm for 1 h at 25°C, then filtered to obtain a filtered residue, which was washed three times with deionized water. Subsequently, calcium hydroxide ($Ca(OH)_2$, 95%,

Macklin) was added to the filtrate to precipitate $SO_4^{2-}$ as $CaSO_4$. The washed residue was dried in a vacuum oven to obtain a powder, which was designated as the oxidized intermediate (O-NCM523). Then, O-NCM523 was uniformly ground with lithium hydroxide monohydrate ($LiOH{\cdot}H_2O$, Ganfeng Lithium Co., Ltd.) to achieve a molar ratio of Li/(Ni + Co + Mn) = 1.2: 1 and then calcined in a muffle furnace at 900 °C for 10 h (heating rate: 5 °C/min, atmosphere: air) to obtain the regenerated material, recorded as R-NCM523. Considering that the Li/TM molar ratio of O-NCM523 is 0.45, an additional 0.75 molar Li was added to reach the target ratio of Li/TM = 1.2. In addition, S-NCM523 powder was mixed with $LiOH{\cdot}H_2O$ to achieve a molar ratio of Li/(Ni + Co + Mn) = 1.2: 1 and calcined in a muffle furnace at 900 °C for 10 h (heating rate: 5 °C/min, atmosphere: air). The regenerated material obtained in this way was named D-NCM523. The oxidation conditions for S-NCM622 and S-NCM811 were the same as those described above, with regeneration temperatures of 850 °C for S-NCM622 and 780 °C for S-NCM811. The commercial poly-crystal material was denoted as C-NCM523. The commercial single-crystal material was denoted as CS-NCM523 (Xinxiang Tianli Lithium Energy Co.), with a tap density of 1.62 g/cm$^3$.

### Material characterizations

The XRD measurements were carried out on an Empyrean model instrument from Panacor in the Netherlands under the following conditions: radiation source Cu Kα (λ = 1.54184 Å), and a measuring range of 10-80°. The in-situ XRD measurements used CR2032 coin cells with a glass window (Wuhan Congtical Technology Co., Ltd). The XRD data were characterized and analyzed using HighScore Plus and GSAS II software. The elemental composition of the materials and solutions was characterized using an inductively coupled plasma emission spectrometer (ICP-OES) from Leeman Labs, USA. The microstructure and morphology of the materials were analyzed using a Nova NanoSEM 450 field-emission scanning electron microscope (SEM) from FEI, USA, and a Tecnai G2 20 and a Talos F200X transmission electron microscope (TEM) from FEI, Netherlands. The elemental distribution analyses by EELS were performed using a Titan G2 60-300 high-resolution STEM microscope from Thermo Fisher Scientific (USA). To obtain the SEM cross sections, the particles were cut using a focused ion beam. X-ray photoelectron spectroscopy (XPS) of AXIS-ULTRA DLD-600W from Shimadzu-Kratos, Japan, was utilized to detect the variation of elements and valence states on the surface of the materials, and combined with Avantage software for analysis. The tap density of the material was tested using an AccuPyc 1340 fully automated true density tester from Anton Paar, Austria, with a vibration frequency of 250 cycles per minute and a total vibration count of 8000 cycles. The variation in functional groups and bond lengths of the materials was investigated using a LabRAM HR800 laser confocal Raman spectrometer (Raman) from Horiba Jobin Yvon. The local structural evolution of the material (atomic occupancy, bond lengths) was measured by the Multi-Physics Spectrometer (MPI) at the China Spallation Neutron Source (CNSNS) and analyzed using the GASA II and PDFgui software. The X-ray absorption spectroscopy (XAS) experiments were performed at beamline P64 Advanced X-ray Absorption Spectroscopy at PETRA III (Germany) and RapidXAFS 2 M X-ray Absorption Spectrometer (Anhui Absorption Spectroscopy Analysis Instrument Co., Ltd.). The obtained XAS data were processed using ATHENA software.

### Theoretical calculations

Our computational framework implements the Vienna Ab Initio Simulation Package (VASP) for density functional theory (DFT). To describe the exchange-correlation function, the generalized gradient approximation (GGA) was utilized in the Perdew-Burke-Ernzerhof (PBE) scheme. The projector augmented wave (PAW) formalism was adopted to model ionic cores, with valence electrons represented through a plane-wave basis set featuring a 500 eV kinetic energy cutoff. Partial occupancies of the Kohn-Sham orbitals were allowed using the Gaussian smearing method with a width of 0.05 eV. For energy variations less than $10^{-5}$ eV, the electron energies were regarded as self-consistent. When the force variation was less than 0.05 eV/Å, the geometry optimization was regarded as convergent. The k-point sampling was performed using gamma points in the Brillouin zone, with all atoms allowed to relax during the structure optimization. Lastly, the nudged elastic band (NEB) approach was used to characterize the Li migration transition state at the path steps. In the NEB approach, pathways between reactants and products were discretized into a series of structural images.

### Electrochemical measurements

For coin cell preparation, NCM powder, carbon black (Super P, 99.9%, TIMCAL), and polyvinylidene fluoride (PVDF900, 99%, Canrd Technology Co., Ltd.) were mixed in a weight ratio of 8:1:1 and dissolved in N-methyl-2-pyrrolidone (NMP, 99%, Aladdin). After stirring for 4 h to achieve a uniform slurry, the slurry was spread onto carbon-coated Al foil (15 μm thick, 99.9%) using a doctor blade and dried in an oven at 80 °C for 6 h. The electrodes were punched into 8 mm discs (0.503 cm$^2$), with a mass loading of 4–6 mg/cm$^2$. CR2032 coin cells were assembled in an Ar-filled glovebox (25 ± 1 °C, $O_2$ and $H_2O$ < 0.01 ppm), using Celgard 2500 (25 μm thick, 19 mm diameter, 55% porosity, from Celgard, USA) as the separator and lithium metal (0.5 mm thick, 12 mm diameter, China Energy Lithium Co., Ltd.) as the negative electrode. Each coin cell was filled with 40 μL of electrolyte (1.0 M $LiPF_6$ in EC: DEC = 1:1 vol%, with 5.0% FEC). The positive and negative cases, along with the nickel foam mesh, were purchased from Canrd Technology Co., Ltd. Cycling was tested at 3.0–4.3 V and 3.0–4.5 V (1 C = 170 mA/g).

Pouch-type full cells with ~1 Ah capacity assembled using R-NCM523 as the positive electrode and graphite as the negative electrode. The positive electrode had a mass loading of ~29.8 mg/cm$^2$ and consisted of 96.5 wt% active material, 1.5 wt% conductive additive, and 2.0 wt% PVDF binder, with an electrode size of 8.0 × 6.0 cm$^2$. The negative electrode had a mass loading of ~16.0 mg cm$^2$ and consisted of 95.4 wt% active material, 2.0 wt% conductive additive, and 2.6 wt% binders, including carboxymethyl cellulose (CMC, Canrd Technology Co., Ltd.) and styrene-butadiene rubber (SBR, Canrd Technology Co., Ltd.), with an electrode size of 8.4 × 6.3 cm$^2$. In the pouch battery, the N/P ratio is 1.15. Approximately 3 mL of electrolyte was uniformly introduced into the pouch cell using a pipette. After sufficient wetting, the cell was transferred to a vacuum sealer. Before final heat sealing, a 5 s degassing step was performed under a vacuum of -98.0 kPa. During cycle testing, an external pressure of ~200 kPa was applied to the pouch cell to ensure stable electrode contact. Cycling performance was tested at 3.0–4.4 V, 1 C. The compacted density, porosity, and volumetric capacity of the positive electrode are shown in Supplementary Fig. 28.

The Princeton electrochemical workstation measured cyclic voltammetry (CV) and electrochemical impedance spectroscopy (EIS) with a voltage range of 3–4.3 V. The CV scan rate ranges from 0.1 to 1.0 mV/s. Additionally, EIS was performed over the frequency range 0.01-100,000 Hz at a signal amplitude of 10 mV. A total of 71 data points were collected within the test frequency range. The Galvanostatic Intermittent Titration Technique (GITT) measurement was conducted with a 10-minute constant-current charge and a 40-minute rest period. All coin cells and pouch batteries were rested for 12 hours to ensure complete electrolyte wetting before electrochemical testing. All electrochemical measurements were conducted at 25 ± 1 °C using NEWARE and Land battery testing systems without a temperature-controlled chamber.

## Data availability

All data are available within the main text and supplementary files, or available from the corresponding authors. Source data are provided with this paper.

## References


1. Ciez, R. E. & Whitacre, J. F. Examining different recycling processes for lithium-ion batteries. *Nat. Sustain.* **2**, 148–156 (2019).
2. Xu, C. et al. Bulk fatigue induced by surface reconstruction in layered Ni-rich cathodes for Li-ion batteries. *Nat Mater.* **20**, 84–92 (2021).
3. Ma, J. et al. Subtractive transformation of cathode materials in spent Li-ion batteries to a low-cobalt 5 V-class cathode material. *Nat. Commun.* **15**, 1046 (2024).
4. Jin, W., Cha, H., Choi, S. & Song, G. Electrode-level strategies for high-Ni cathodes in high-energy-density batteries beyond material design. *Energy Mater* **5**, 500130 (2025).
5. Ji, G. et al. Direct regeneration of degraded lithium-ion battery cathodes with a multifunctional organic lithium salt. *Nat. Commun.* **14**, 584 (2023).
6. Zeng, Z. et al. Large-scale and homogenized strategies of spent $LiFePO_4$ recycling: reconstruction of targeted lattice. *Adv. Funct. Mater.* **34**, 2308671 (2023).
7. Kong, Y. L. et al. Efficient separation and selective Li recycling of spent $LiFePO_4$ cathode. *Energy Mater* **3**, 300053 (2023).
8. Shan, M. et al. Recycling of $LiFePO_4$ cathode materials: From laboratory scale to industrial production. *Mater. Today* **73**, 130–150 (2024).
9. Yang, T., Luo, D., Yu, A. & Chen, Z. Enabling future closed-loop recycling of spent lithium-ion batteries: direct cathode regeneration. *Adv. Mater.* **35**, 2203218 (2023).
10. Chi, Z. et al. Direct regeneration method of spent $LiNi_{1/3}Co_{1/3}Mn_{1/3}O_2$ cathode materials via surface lithium residues. *Green Chem* **23**, 9099–9108 (2021).
11. Zhang, N., Deng, W., Xu, Z. & Wang, X. Upcycling of spent $LiCoO_2$ cathodes via nickel- and manganese-doping. Carbon. *Energy* **5**, 1–10 (2022).
12. Xu, P. P. et al. Efficient Direct Recycling of Lithium-Ion Battery Cathodes by Targeted Healing. *Joule* **4**, 2609–2626 (2020).
13. Gao, H. et al. Upcycling of spent $LiNi_{0.33}Co_{0.33}Mn_{0.33}O_2$ to single-crystal ni-rich cathodes using lean precursors. *ACS Energy Lett* **8**, 4136–4144 (2023).
14. Hao, S. P. et al. Restoration of $Li^+$ pathways in the [010] direction during direct regeneration for spent $LiFePO_4$. *Energy Environ. Sci.* **18**, 3750–3760 (2025).
15. Dong, H. et al. Single-crystal materials regenerated and modified by spent ncm523 as a high-voltage stable cycling cathode material. *ACS Sustain. Chem. Eng.* **10**, 11587–11596 (2022).
16. Gupta, V. et al. Scalable direct recycling of cathode black mass from spent lithium-ion batteries. *Adv. Energy Mater.* **13**, 2203093 (2022).
17. Gong, H. et al. Noninvasive rejuvenation strategy of nickel-rich layered positive electrode for Li-ion battery through magneto-electrochemical synergistic activation. *Nat. Commun.* **15**, 10243 (2024).
18. Jin, Y., Zhang, T. & Zhang, M. Advances in intelligent regeneration of cathode materials for sustainable lithium-ion batteries. *Adv. Energy Mater.* **12**, 2201526 (2022).
19. Xiao, Z. et al. Strong oxidizing molten salts for strengthening structural restoration, enabling direct regeneration of spent layered cathode. *Small* **20**, e2309685 (2024).
20. Liu, X. et al. Organic eutectic salts-assisted direct lithium regeneration for extremely low state of health ni-rich cathodes. *Adv. Energy Mater.* **13**, 2302987 (2023).
21. Xu, M. et al. Direct regeneration of spent $LiCoO_2$ black mass based on fluorenone-mediated lithium supplementation and energy-saving structural restoration. *Adv. Energy Mater.* **14**, 2401197 (2024).
22. Yu, X. et al. Achieving low-temperature hydrothermal relithiation by redox mediation for direct recycling of spent lithium-ion battery cathodes. *Energy Storage Mater* **51**, 54–62 (2022).
23. Ji, H., Wang, J., Ma, J., Cheng, H.-M. & Zhou, G. Fundamentals, status and challenges of direct recycling technologies for lithium ion batteries. *Chem. Soc. Rev.* **52**, 8194–8244 (2023).
24. Qin, Z. et al. A ternary molten salt approach for direct regeneration of $LiNi_{0.5}Co_{0.2}Mn_{0.3}O_2$ cathode. *Small* **18**, 2106719 (2022).
25. Bhattacharya, S., Mukherjee, R. & Chakravorty, A. A Nickel(III) Complex with a $NiO_6$ coordination sphere. *Inorg. Chem.* **25**, 3448–3452 (1986).
26. Zrinyi, N. & Pham, A. L.-T. Oxidation of benzoic acid by heat-activated persulfate: Effect of temperature on transformation pathway and product distribution. *Water Res* **120**, 43–51 (2017).
27. Zhu, G., Fan, X., Yu, Y., Liu, Y. & Quan, X. Regulating the electronic structure of cu single-atom catalysts toward enhanced electro-fenton degradation of organic contaminants via $^1O_2$ and ·OH. *Environ. Sci. Technol.* **58**, 19545–19554 (2024).
28. Tsitonaki, A., Smets, B. F. & Bjerg, P. L. Effects of heat-activated persulfate oxidation on soil microorganisms. *Water Res* **42**, 1013–1022 (2008).
29. Song, S. H. et al. Rational design of Li off-stoichiometric Ni-rich layered cathode materials for Li-ion batteries. *Chem. Eng. J.* **448**, 137685 (2022).
30. Li, J. Y. et al. In-situ probing the near-surface structural thermal stability of high-nickel layered cathode materials. *Energy Storage Mater* **46**, 90–99 (2022).
31. Anspoks, A. & Kuzmin, A. Interpretation of the Ni K-edge EXAFS in nanocrystalline nickel oxide using molecular dynamics simulations. *J. Non-Cryst. Solids* **357**, 2604–2610 (2011).
32. Yao, Z. et al. Modulating the spin state to stabilize the surface and bulk structure for durable 4.6 V $LiCoO_2$ Cathodes. *Adv. Funct. Mater.* **34**, 2408152 (2024).
33. Zhang, M. J. et al. Cationic ordering coupled to reconstruction of basic building units during synthesis of high-ni layered oxides. *J Am Chem Soc* **140**, 12484–12492 (2018).
34. Zhang, J. et al. Probing the nature of $Li^+/Ni^{2+}$ disorder on the structure and electrochemical performance in ni-based layered oxide cathodes. *Journal of The Electrochemical Society* **166**, A4097–A4105 (2019).
35. Kawaguchi, T. et al. Roles of transition metals interchanging with lithium in electrode materials. *PCCP* **17**, 14064–14070 (2015).
36. Kang, J. et al. Realizing two-electron transfer in Ni $(OH)_2$ nanosheets for energy storage. *J. Am. Chem. Soc.* **144**, 8969–8976 (2022).
37. He, Z. D., Tesch, R., Eslamibidgoli, M. J., Eikerling, M. H. & Kowalski, P. M. Low-spin state of Fe in Fe-doped NiOOH electrocatalysts. *Nat. Commun.* **14**, 3498 (2023).
38. Zhang, Y. et al. Upcycling of high-rate Ni-rich cathodes through intrinsic structural features. *Adv. Energy Mater.* **14**, 2402918 (2024).
39. Fujita, Y., Amine, K., Maruta, J. & Yasuda, H. $LiNi_{1-x}Co_xO_2$ prepared at low temperature using β-$Ni_{1-x}Co_xOOH$ and either $LiNO_3$ or LiOH. *J. Power Sources* **68**, 126–130 (1997).
40. Wang, H. et al. Tandem topotactic reactions for low-temperature synthesis of ni-rich layered oxide cathodes without anti-site defect. *J. Am. Chem. Soc.* **147**, 35355–35366 (2025).
41. Adipranoto, D. S. et al. Crystal-local structure analyses for cathode LIBs $LiNi_{1-x}Co_xO_2$ ($0 \le x \le 1$) by neutron diffraction. *In: JPS Conference Proceedings* **8**, 031017 (2015).
42. Zheng, J. M., Yan, P. F., Estevez, L., Wang, C. M. & Zhang, J. G. Effect of calcination temperature on the electrochemical properties of nickel-rich $LiNi_{0.76}Mn_{0.14}Co_{0.10}O_2$ cathodes for lithium-ion batteries. *Nano Energy* **49**, 538–548 (2018).

43. Wu, V. C. et al. High energy density and micrometer-sized $d^0$-free disordered rocksalt cathodes. *Energy Environ. Sci.* **18**, 8918–8928 (2025).
44. Han, D. Z. et al. Enhancing the long-term cycling stability of Ni-rich cathodes via regulating the length/width ratio of primary particle. *Energy Mater* **4**, 400001 (2024).
45. Jeevanantham, B. & Shobana, M. K. Systematic electrochemical analysis of high-capacity NMC-88 and NMC-83 cathodes for lithium-ion batteries. *Journal of Materials Science: Materials in Electronics* **35**, 2049 (2024).
46. Wang, J. et al. Direct recycling of spent cathode material at ambient conditions via spontaneous lithiation. *Nat. Sustain.* **7**, 1283–1293 (2024).
47. Huang, Q. et al. Surface engineering enabling efficient upcycling of highly degraded layered cathodes. *Adv. Mater.* **37**, 2419872 (2025).
48. Zhuang, Z. et al. Fast Li replenishment channels-assisted recycling of degraded layered cathodes with enhanced cycling performance and thermal stability. *Adv. Mater.* **36**, 2313144 (2024).
49. Fan, M. et al. Reviving fatigue surface for solid-state upcycling of highly degraded polycrystalline $LiNi_{1-x-y}Co_xMn_yO_2$ Cathodes. *Adv. Mater.* **36**, 2405238 (2024).
50. Wang, W. et al. Upcycling spent $LiNi_{0.55}Co_{0.15}Mn_{0.3}O_2$ battery cathode via high-valence-element oxide surface engineering. *ACS Energy Lett* **10**, 1577–1584 (2025).
51. Jia, K. et al. Topotactic transformation of surface structure enabling direct regeneration of spent lithium-ion battery cathodes. *J. Am. Chem. Soc.* **145**, 7288–7300 (2023).
52. Ma, J. et al. Adaptable eutectic salt for the direct recycling of highly degraded layer cathodes. *J. Am. Chem. Soc.* **144**, 20306–20314 (2022).
53. Chen, Z. et al. Reaction-passivation mechanism driven materials separation for recycling of spent lithium-ion batteries. *Nat. Commun.* **14**, 4648 (2023).
54. Jin, S. et al. Facilitating cathode regeneration via defect-driven prelithiation. *Adv. Funct. Mater.* **35**, 2416085 (2024).
55. Chen, L. et al. Effective upcycling of degraded ncm cathode materials assisted by surface engineering for high-performance lithium-ion batteries. *Adv. Funct. Mater.* **35**, 2411182 (2024).


## Acknowledgements

This work was supported by the National Key Research and Development Program of China (2025YFF0516300 [L.Y.]), the National Natural Science Foundation of China (NSFC, Grant Nos. 22479058 [L.Y.], 12205325 [W.L.]) and the Key R&D Program of Hubei Province (2024BCB091 [L.Y.]). We thank the staff members of the Multi-Physics Instrument Neutron Scattering (https://cstr.cn/31113. 02. CSNS. MPI) at the China Spallation Neutron Source (CSNS) (https://cstr.cn/31113. 02. CSNS), for providing technical support and assistance in data collection and analysis.

## Author contributions

S. H. conducted the experiments and prepared the manuscript. Y.Z., S.L., Z.T., W.L., Y.X., and W.Y. contributed to the completion of part of the characterizations. Y.L. (Yaqi Liao), H.J., Y. K., Y.S., and Y.L. (Yuelin Lv) gave instructive advice to perform the experiments. L.Q., Y.H. and L.Y. conceived and designed the research. All authors contributed to the discussion of the manuscript.

## Competing interests

The authors declare no competing interests.

## Additional information

**Supplementary information** The online version contains supplementary material available at https://doi.org/10.1038/s41467-026-71730-3.

**Correspondence** and requests for materials should be addressed to Long Qie, Yunhui Huang or Lixia Yuan.

**Peer review information** *Nature Communications* thanks Jinhui Li, and the other, anonymous, reviewer(s) for their contribution to the peer review of this work. A peer review file is available.

**Reprints and permissions information** is available at http://www.nature.com/reprints

**Publisher's note** Springer Nature remains neutral with regard to jurisdictional claims in published maps and institutional affiliations.

**Open Access** This article is licensed under a Creative Commons Attribution-NonCommercial-NoDerivatives 4.0 International License, which permits any non-commercial use, sharing, distribution and reproduction in any medium or format, as long as you give appropriate credit to the original author(s) and the source, provide a link to the Creative Commons licence, and indicate if you modified the licensed material. You do not have permission under this licence to share adapted material derived from this article or parts of it. The images or other third party material in this article are included in the article's Creative Commons licence, unless indicated otherwise in a credit line to the material. If material is not included in the article's Creative Commons licence and your intended use is not permitted by statutory regulation or exceeds the permitted use, you will need to obtain permission directly from the copyright holder. To view a copy of this licence, visit http://creativecommons.org/licenses/by-nc-nd/4.0/.

© The Author(s) 2026